Supporting Information

A novel nanocomposite of mesoporous silica supported Ni nanocrystals modified by ceria clusters with extremely high light-to-fuel efficiency for UV-Vis-IR light-driven CO_2 reduction

Zhongkai Jiang, Yuanzhi Li,* Qian Zhang, Yi Yang, Shaowen Wu, Jichun Wu, Xiujian Zhao

State Key Laboratory of Silicate Materials for Architectures (Wuhan University of Technology), 122 Luoshi Road, Wuhan 430070, P. R. China. Email: liyuanzhi66@hotmail.com

Table S1. Comparison of catalytic activity and light-to-fuel efficiency of different CO_2 reduction strategies.

Methods	Catalyst	Light intensity (kWm^{-2})	CO production rate		Light-to-fuel efficiency (%)	Reference
			Reported	Calculated (mmol min^{-1} g^{-1})[a]		
Solar thermochemical CO_2 dissociation	porous monolithic CeO_2	1500	1500 mL min^{-1}	0.206	0.8	[1] *Science*, 2010, 330, 1797
Solar thermochemical CO_2 dissociation	Reticulated porous ceramic foam of CeO_2	3000	1.2 mL·min^{-1} g^{-1}	0.054	5.25	[2] *Energy Environ. Sci.*, 2017, 10, 1142
Photocatalytic CO_2 reduction by H_2O	Hierarchical treated rape pollen	2.5	845.7 μmol h^{-1} g^{-1}	0.014	6.7 [e]	[4] *Energy Environ. Sci.*, 2018, 11, 2382
Photocatalytic CO_2 reduction by H_2O	hierarchical NC@$NiCo_2O_4$	no data provided	2.62×10^4 μmol h^{-1} g^{-1}	0.44	1.07 [e]	[11] *Energy. Environ. Sci.*, 2018, 11, 306
Photoelectrochemical CO_2 reduction by H_2O	Copper iron oxide electrode	1	5 μmol h^{-1}	3.33×10^{-4} [b]	1	[22] *Energy Environ. Sci.*, 2015, 8, 2638
Photothermocatalytic CO_2 reduction by H_2	Ru/Si nanowires	3.2	0.80 mmol g^{-1} h^{-1}	0.0133 [c]	*no data*[f]	[25] *Adv. Sci.*, 2014, 1, 1400001
Light-driven thermocatalytic CO_2 reduction by CH_4	Silica cluster modified Ni nanocrystals	343.6		19.9, 17.1[d]	12.5	[31a] *Adv. Energy Mater.*, 2018, 1702472.
Light-driven thermocatalytic CO_2 reduction by CH_4	Ceria cluster modified Ni nanocrystals	385.2		41.53, 33.42[d]	27.4	In this work

Note: [a] The values are calculated according to the reported data, [b] formate production rate (mmol min^{-1} cm^{-2}), [c] CH_4 production rate, [d] H_2 production rate, [e] quantum efficiency at 420 nm (no light-to-fuel efficiency was provided), [f] Light-to-fuel conversion could not be realized by the strategy due to the exothermic characteristics of CO_2 reduction by H_2 (e. g. $CO_2+4H_2=CH_4+2H_2O$, ΔG_{298}= -113.3 kJ mol^{-1}).

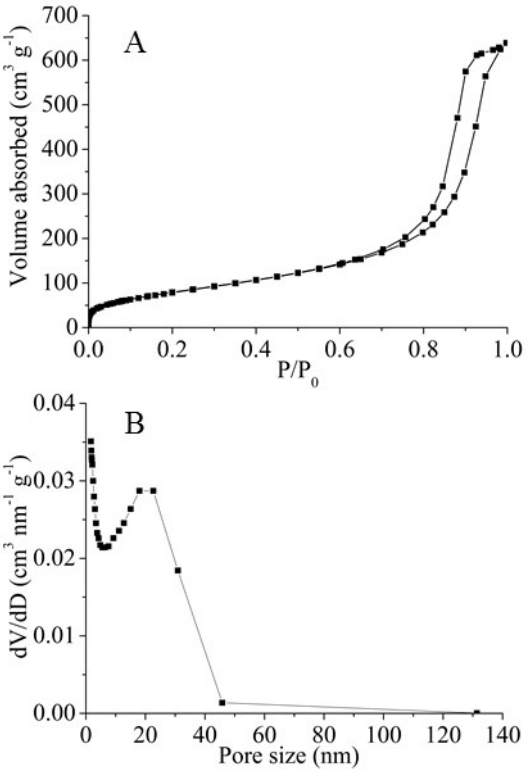

Figure S1. N_2 adsorption and desorption (A) and BJH adsorption pore size distribution (B) of Ni-CeO_2/SiO_2.

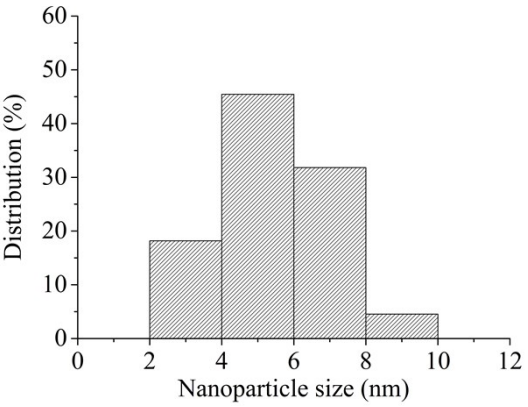

Figure S2. Size distribution of Ni nanoparticles in Ni-CeO_2/SiO_2 by TEM.

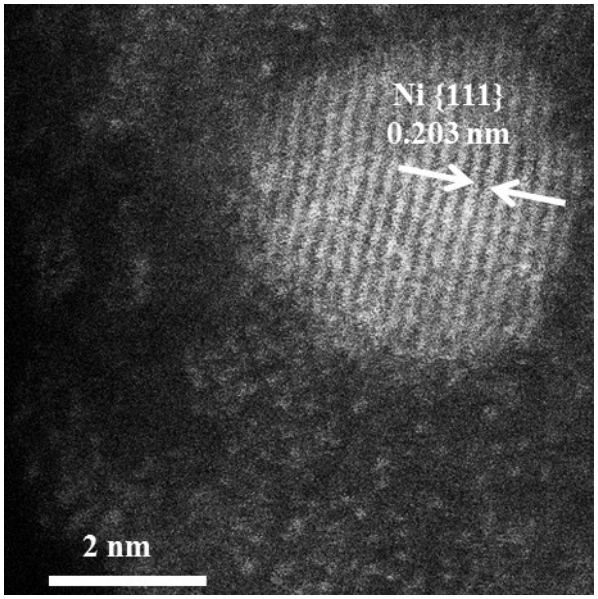

Figure S3. High resolution HAADF image of Ni-CeO_2/SiO_2. As shown in Ni mapping (Figure 1D), Ni in Ni-CeO_2/SiO_2 exists in the form of Ni nanoparticles without randomly distributed Ni species. Therefore, randomly distributed bright dots (the lower part of the image) are Ce atoms in ceria clusters on silica. Similar bright dots are orderly distributed on a Ni nanocrystal. The orderly distributed bright dots are ascribed to Ce atoms in ceria clusters rather than Ni atoms in Ni nanocrystal. The reason is follows: As shown in the element mappings of Ni and Ce (Figure 1C and 1D), Ce atoms are well distributed on Ni nanocrystals. In HAADF image, the bright dots of Ce atoms have higher brightness than the dots of Ni atom due to the atomic number of Ce (58) much larger than that of Ni (28) according to the principle of HAADF.

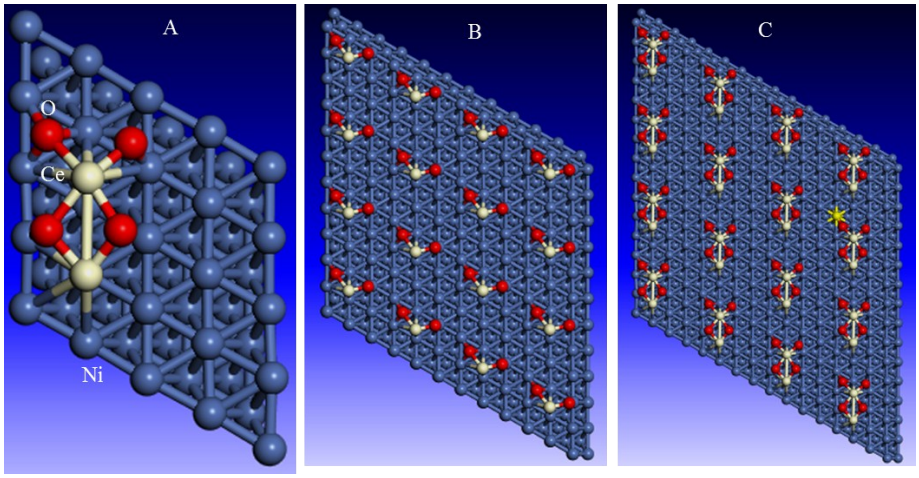

Figure S4. Geometry of the $(CeO_2)_2/Ni_{48}$ slab (A), and periodic configurations of the CeO_2/Ni_{48} slab (B), and the $(CeO_2)_2/Ni_{48}$ slab (C).

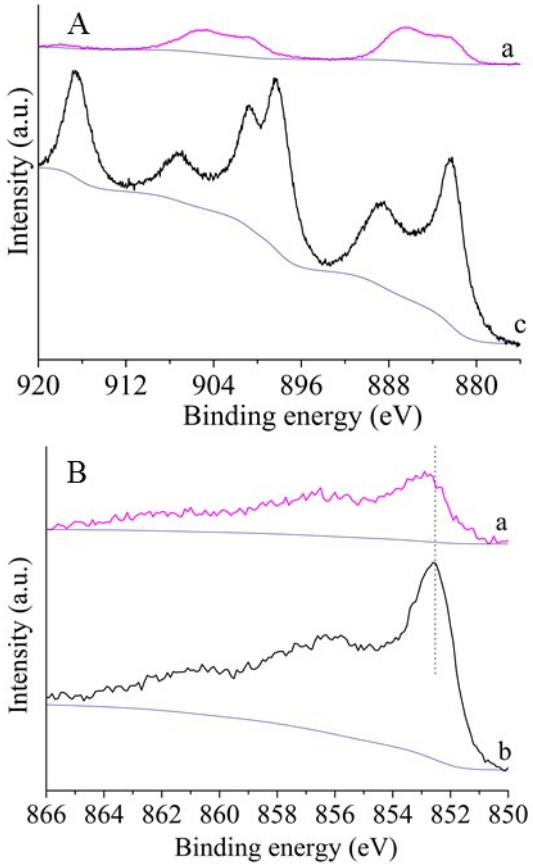

Figure S5. Ce3d (A) and Ni2p3/2 (B) spectra of Ni-CeO_2/SiO_2 (a), Ni/SiO_2 (b), and CeO_2 (c).

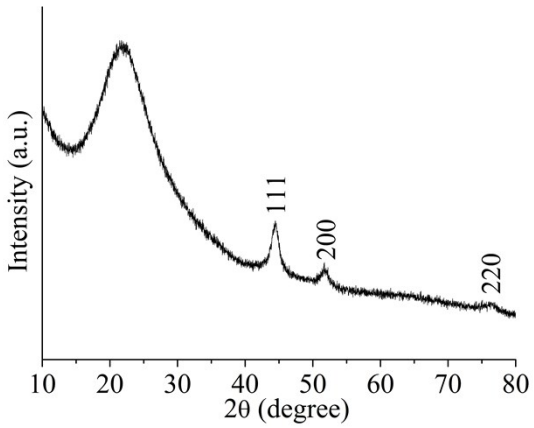

Figure S6. XRD patterns of Ni/SiO_2. Ni/SiO_2 shows XRD peaks of crystalline metallic Ni (JCPDS 65-2865). SiO_2 exists in amorphous silica evidenced by a broad peak in the range of 15~30°. The average size of Ni nanocrystals in the nanocomposite, calculated in accordance to the Scherrer formula ($L=0.89\lambda/\beta\cos\theta$) at the peak of {111} facets ($2\theta = 44.5°$), is 7.3 nm.

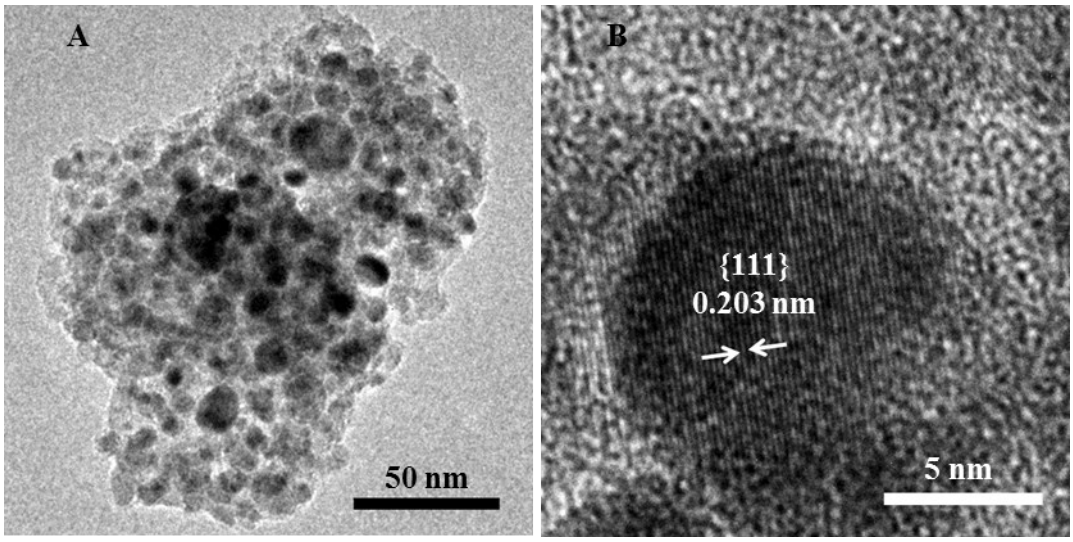

Figure S7. TEM image (A) and HRTEM image (B) of Ni/SiO_2. HRTEM image demonstrates that Ni nanocrystal surrounded by amorphous silica has clear lattice spacing of {111} facets (0.203 nm).

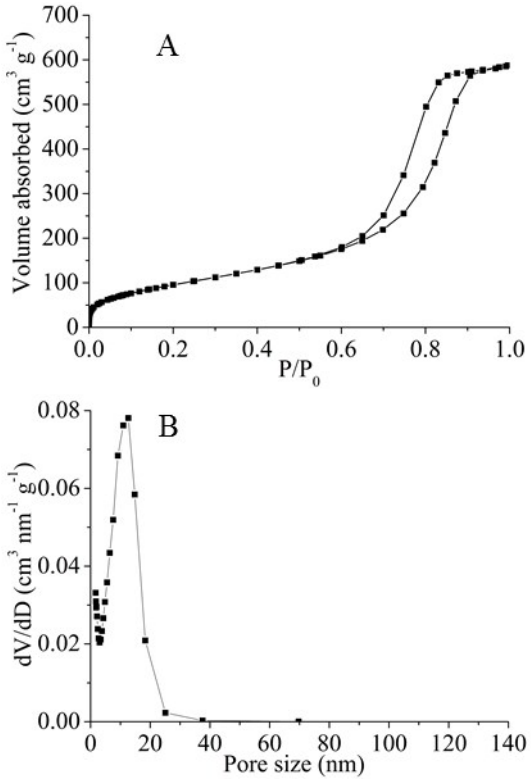

Figure S8. N_2 adsorption and desorption (A) and BJH adsorption pore size distribution (B) of Ni/SiO_2.

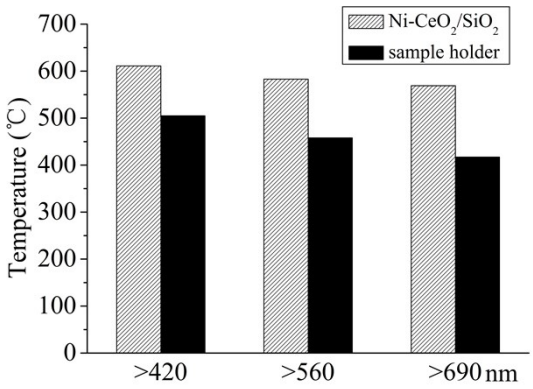

Figure S9. The T_{eq} values of $Ni\text{-}CeO_2/SiO_2$ and the sample holder surface (without catalyst) under the focused visible-infrared illumination.

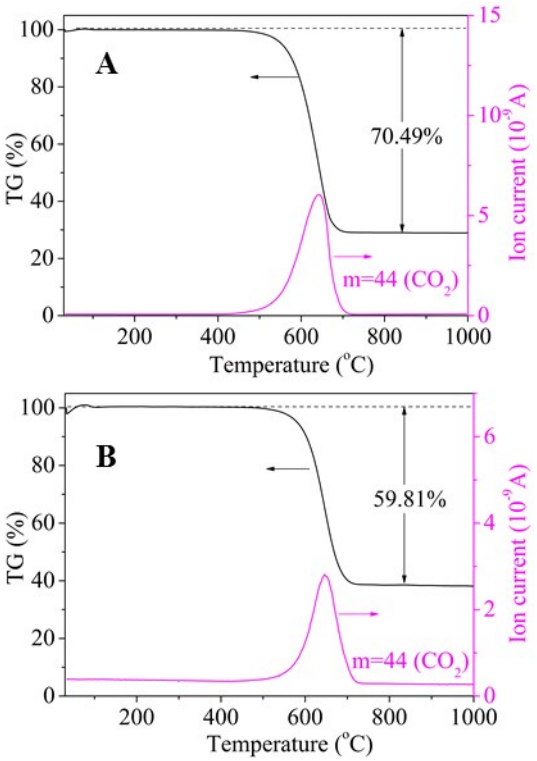

Figure S10. TG-MS profiles of the used Ni-CeO_2/SiO_2 catalyst after 100 h CRM reaction under focused UV-visible-infrared illumination (A) and the used Ni/SiO_2 catalyst after 4 h CRM reaction under focused UV-visible-infrared illumination (B).

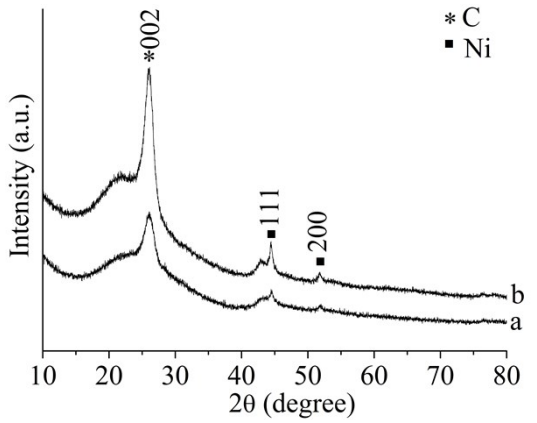

Figure S11. XRD patterns of the used Ni-CeO_2/SiO_2 catalyst after 100 h CRM reaction under focused UV-visible-infrared illumination (a) and the used Ni/SiO_2 catalyst after 4 h CRM reaction under focused UV-visible-infrared illumination (b): * represents graphite 2H (PDF 75-1621).

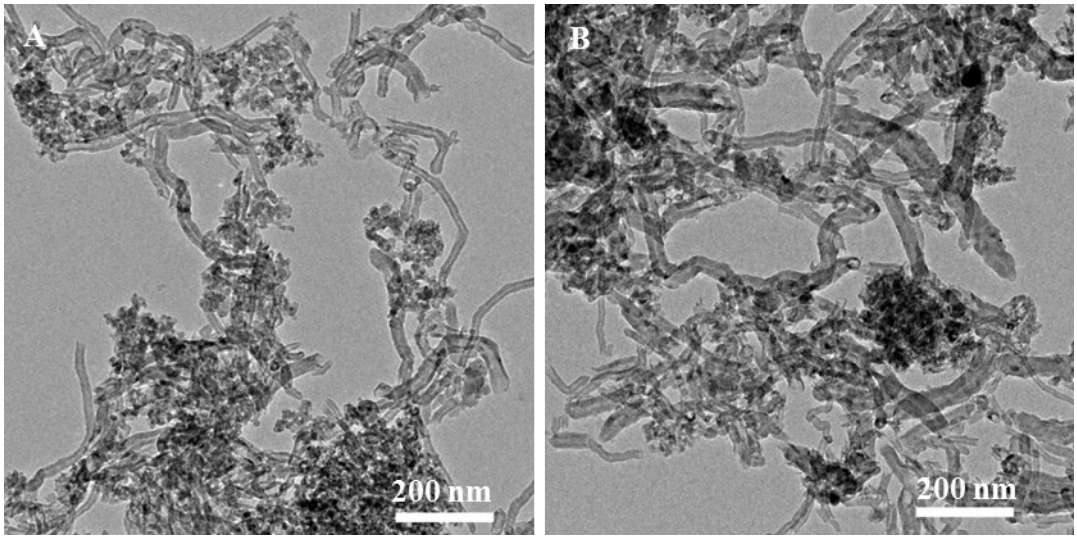

Figure S12. TEM images of the used Ni-CeO_2/SiO_2 catalyst after 100 h CRM reaction under focused UV-visible-infrared illumination (A) and the used Ni/SiO_2 catalyst after 4 h CRM reaction under focused UV-visible-infrared illumination (B).

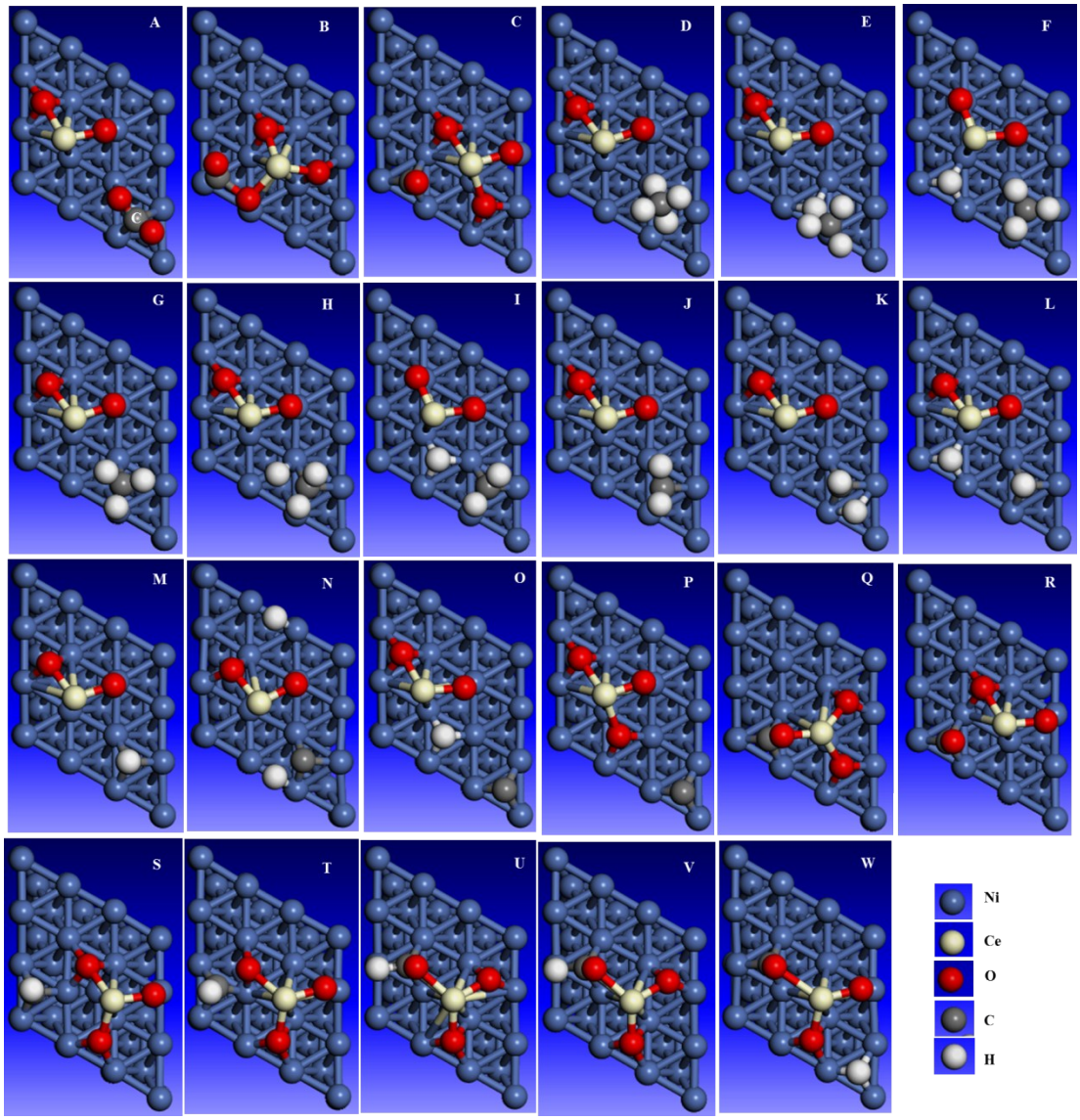

Figure S13. Geometries of the initial states, transition states, and intermediates for CRM on the CeO_2/Ni_{36} slab in the ground states: chemisorbed CO_2 (A), transition state of CO_2 dissociation (B), intermediate of CO_2 dissociation(C), chemisorbed CH_4 (D), transition state of CH_4 dissociation(E), intermediate of CH_4 dissociation(F), chemisorbed CH_3(G), transition state of CH_3 dissociation(H), intermediate of CH_3 dissociation(I), chemisorbed CH_2 (J), transition state for CH_2 dissociation (K), intermediate of CH_2 dissociation (L), chemisorbed CH (M), transition state CH dissociation (N), intermediate of CH dissociation (O), chemisorbed intermediate of C and O (P), transition state of C oxidation (Q), chemisorbed CO (R), chemisorbed intermediate of CH and O (S), transition state of CH oxidation (T), intermediate of CHO by CH oxidation (U), transition state of CHO dissociation (V), and intermediate of CO and H by CHO dissociation (W).

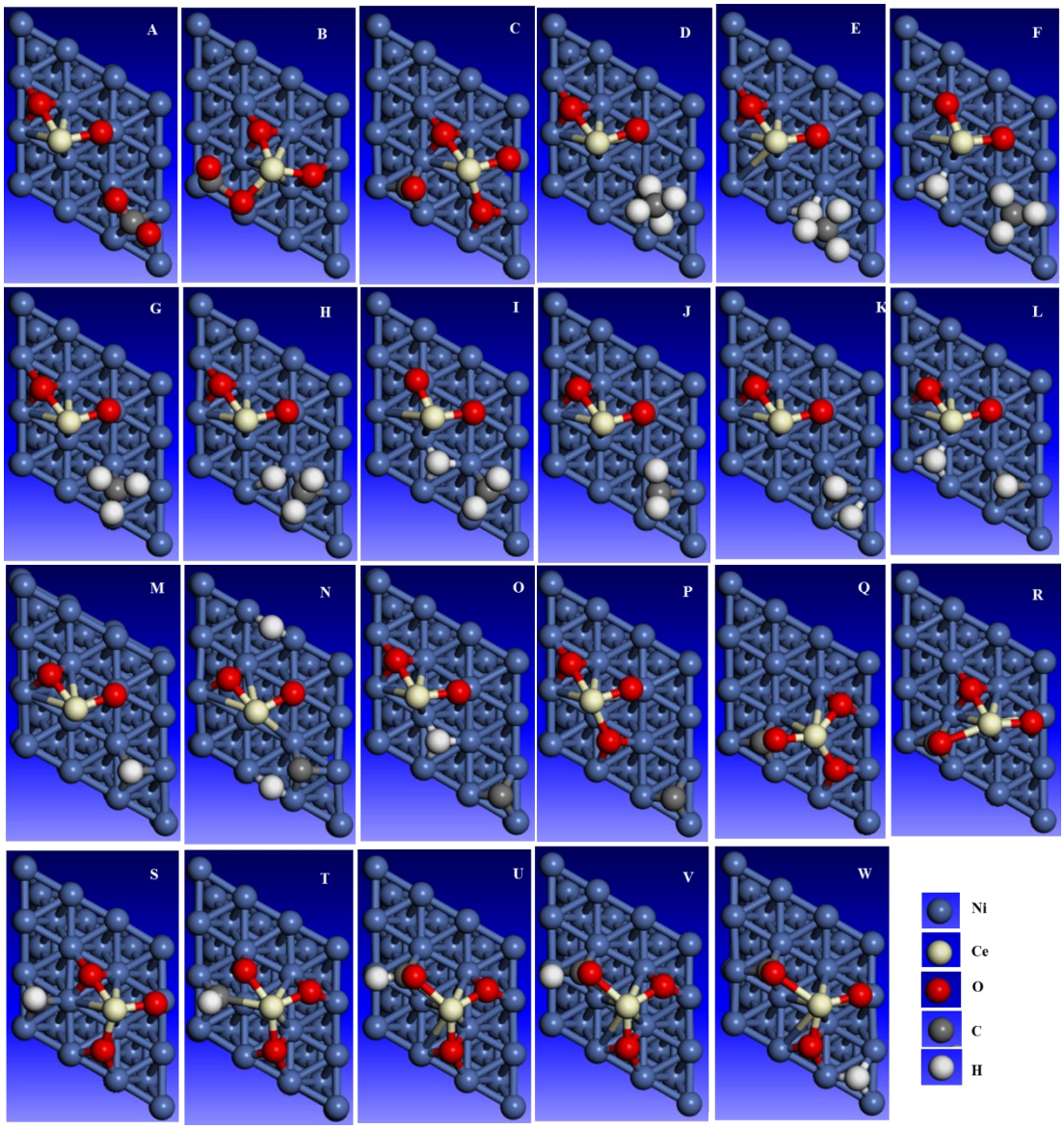

Figure S14. Geometries of the initial states, transition states, and intermediates for CRM on the CeO_2/Ni_{36} slab in the excited states: chemisorbed CO_2 (A), transition state of CO_2 dissociation (B), intermediate of CO_2 dissociation(C), chemisorbed CH_4 (D), transition state of CH_4 dissociation(E), intermediate of CH_4 dissociation(F), chemisorbed CH_3(G), transition state of CH_3 dissociation(H), intermediate of CH_3 dissociation(I), chemisorbed CH_2 (J), transition state for CH_2 dissociation (K), intermediate of CH_2 dissociation (L), chemisorbed CH (M), transition state CH dissociation (N), intermediate of CH dissociation (O), chemisorbed intermediate of C and O (P), transition state of C oxidation (Q), chemisorbed CO (R), chemisorbed intermediate of CH and O (S), transition state of CH oxidation (T), intermediate of CHO by CH oxidation (U), transition state of CHO dissociation (V), and intermediate of CO and H by CHO dissociation (W).

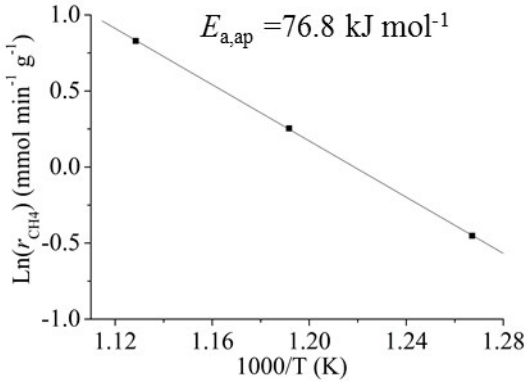

Figure S15. Ln (r_{CH4}) vs 1/T (B) for CRM on the nanocomposite of Ni nanocrystals closely contacted by CeO_2 nanocrystals (Ni/CeO_2, in Ref. 31b) under the focused UV-visible-infrared illumination.